Hot Deformation Behavior and Workability of As-Cast Dilute Mg-1.2Zn-0.2Y Alloy

XU ZHIMING,[1] CHEN XINRONG,[1] YAO BIN,[1] TENG JIE,[1,3]
JIANG FULIN,[1] FU DINGFA,[1] ZHANG HUI,[1] and CHEN CHAOYI[2,4]

1.—College of Materials Science and Engineering, Hunan University, Changsha 410082, People's Republic of China. 2.—College of Materials and Metallurgy, Guizhou University, Guiyang 550025, People's Republic of China. 3.—e-mail: tengjie@hnu.edu.cn. 4.—e-mail: ccy197715@126.com

Flow stress behavior of as-cast dilute Mg-1.2Zn-0.2Y alloy was studied via uniaxial compression test at temperature (300–450°C) and strain rate (0.001–1 s^{-1}) using a Gleeble-3500 thermal simulation tester. The constitutive equation with the deformation activation energy of 275.9 kJ/mol was established to describe the thermal deformation behavior of the tested material. The processing maps for the Mg alloy were also constructed based on dynamic material modeling. Optical microscopy, x-ray diffraction, transmission electron microscopy and electron backscatter diffraction were utilized to characterize the microstructures formed at elevated temperature. The results indicated that dynamic recovery was the dominant work-softening mechanism of the Mg-1.2Zn-0.2Y alloy at lower temperature and dynamic recrystallization mainly contributed to the deformation softening at higher temperature. The optimal processing parameters of the safe deformation window were identified as temperature of 420–450°C and strain rate of 0.001–0.01 s^{-1}.

INTRODUCTION

Magnesium (Mg) alloys, as the lightest commercialized metallic structural material, are receiving great attention and have great potential applications in the automobile, space and aeronautics, and electronics industries owing to their unique physical performances, such as excellent damping ability and high recycle capacity.[1]

In industry, Mg alloys are usually divided into wrought and casting alloys. Although casting alloys account for a large proportion of all Mg alloy products because of the cost advantage of casting alloys over wrought alloys, developing a wrought alloy is attracting much attention and is an important way to expand its applications.[2] For example, the development of ZK60, as a typical high-strength wrought alloy, can be traced back to the 1960s.

It has been reported that the addition of rare earth (RE) elements can remarkably refine the microstructures of Mg alloys and improve their mechanical properties.[3] For example, the addition of gadolinium (Gd) can remarkably improve the heat resistance and high strength of Mg alloys;[4–7] the addition of yttrium (Y) can also refine the microstructure of Mg alloys and improve the strength.[8–10] For Mg-Zn-Y alloys, the icosahedral quasicrystalline phase (I-phase, Mg_3Zn_6Y) can be observed. I-phase is a ternary equilibrium phase and can enhance Mg alloys' properties because of its unique intrinsic properties such as higher hardness and strength, directional relationship and low interface energy with the α-Mg matrix.[11] After subsequent forging processing, Mg alloys can achieve good strengths with moderate ductility by dispersion of Mg_3Zn_6Y-phase.[12,13] Therefore, the existence of I phase is conducive to enhancing Mg alloys' performance at ambient and elevated temperatures.[8,9,14,15] As reported in relevant papers, I phase is more likely to be formed when the ratio of zinc to yttrium is about 6.[8,10,12]

In recent years, many engineers and scientists have devoted much attention to the development of dilute Mg alloys and successfully developed several kinds of dilute Mg alloys, which achieve a perfect balance of ductility and strength by subsequent plastic processing. One of the advantages of the dilute Mg alloy is that it can reduce the addition of alloy elements, thereby greatly reducing the cost of alloys.[16,17]

It is commonly accepted that Mg alloys' microstructure adjustment and mechanical performance improvement can be achieved by hot plastic processing techniques such as heat extrusion, forging and rolling. However, the workability of Mg and its alloys is poor at low temperatures owing to the limited slip systems of the Mg alloy resulting from its hexagonal close-packed (HCP) crystal structure. Therefore, activating additional slip systems by hot processing at elevated temperatures is necessary and can greatly enhance the workability of Mg alloys.[18,19] In addition, the casting microstructure can be effectively adjusted by recrystallization or recovery after hot deformation, which finally improves Mg alloys' mechanical properties.[20–23] Hence, it is important to investigate Mg alloys' hot deformation characteristic and construct their processing maps to optimize the thermal processing parameters. However, previous studies mainly focus on the microstructure and mechanical properties of ZK series Mg alloys[24,25] or AZ series Mg alloys.[26–29]

To the authors' knowledge, the thermal deformation behavior and workability of as-cast dilute Mg-1.2Zn-0.2Y alloy has never been studied so far, and the aim of this article is to investigate its thermal flow behavior using hot compression tests. Furthermore, microstructure observation and processing maps are also adopted to optimize the hot processing parameters.

MATERIALS AND EXPERIMENTAL PROCEDURES

Dilute Mg-Zn-Y alloy was used in the present work, and its chemical compositions (mass fraction) are as follows: 1.2% Zn, 0.2% Y and the balance Mg.

The tested alloy was made by melting high-purity magnesium, zinc and master alloy Mg–30%Y in an electric resistance furnace under the protection of SF_6 and CO_2 mixed gas. Mg billets were completely melted at 800°C, and then zinc and Mg-30%Y were subsequently added into the melt, followed by homogeneous stirring and keeping for 30 min. Then, the melt was cooled to 680°C and poured into a steel mold preheated to 200°C. The Mg-Zn-Y alloy ingots of $\emptyset$ 40 mm × 75 mm were successfully fabricated and homogenized at 400°C for 10 h.

All specimens of $\emptyset$ 10 mm × 15 mm were machined from the middle part of the ingots along the axial line. The uniaxial thermal compression test was conducted at various temperatures (300°C, 350°C, 400°C, 450°C) and strain rates (0.001 s^{-1}, 0.01 s^{-1}, 0.1 s^{-1}, 1 s^{-1}) using a Gleeble-3500 test system. Prior to compression testing, all the specimens were heated up to target temperature with a heating rate of 10°C/s and were then kept for 180 s to obtain temperature stabilization. Graphite lubrication was applied on the sample surface to eliminate the effect of friction formed during compression as far as possible. Once the true strain reached 0.6

during the test, the compression process stopped and the specimen was water-quenched immediately to freeze the deformed microstructure.

Optical microscopy (OM), x-ray diffraction (XRD), transmission electron microscopy (TEM) and electron backscatter diffraction (EBSD) were used to characterize the microstructures of the deformed specimens.

RESULTS AND DISCUSSION

As-Homogenized Microstructure

Figure 1 shows the microstructure of the Mg-1.2Zn-0.2Y alloy homogenized at 400°C for 10 h. In Fig. 1a, the equiaxed grains with an average size of about 300 μm were formed in the Mg alloy after homogenization. The XRD spectrum of the tested Mg alloy is presented in Fig. 1b, which indicates that the Mg alloy mainly consists of α-Mg as well as a very small amount of I phase (Mg_3Zn_6Y) and Z phase ($Mg_{12}ZnY$). As reported in the Ref. 25, the as-cast Mg-Zn-Y series alloy usually forms ternary Mg–Zn–Y phases such as W-phase ($Mg_3Zn_3Y_2$), I-phase (Mg_3Zn_6Y) and Z-phase ($Mg_{12}ZnY$), depending on the equilibrium condition and the Y/Zn mole ratio. The low content of Y is the main reason why I phase is difficult to detect by XRD. In addition, Fig. 1c shows that a small number of twins were formed. Such twins may be induced due to grinding and polishing during the preparation before EBSD measurement. The inverse pole figures (IPF) show the formation of a weak texture with only a maximum intensity of 3.29 above random (Fig. 1d).

Flow Stress Behavior

The true stress–true strain curves under various deformation conditions are presented in Fig. 2. It can be observed that at the initial stage of deformation, the stress value increased sharply with increasing strain and then gradually increased to a maximum value. As the true strain increased further, the flow stress remained stable or slightly decreased. Additionally, it was obvious that the flow stress behavior was significantly affected by the hot deformation parameters. For example, the flow stress value of the tested Mg alloy deformed at the higher strain rates and lower temperatures was higher and vice versa. Supplementary Table S-I (refer to online supplementary material) lists the peak stress values at various deformation conditions.

The true stress–true strain curves also delivered some information about hot deformation mechanisms. As the true strain was < 0.05, work hardening resulting from dislocation generation and multiplication played a key role during deformation and led to a sharp increase in flow stress, as shown in Fig. 2. Then, the increased rate of flow stress decreased, and the flow stress value gradually increased with a further increase of the strain,
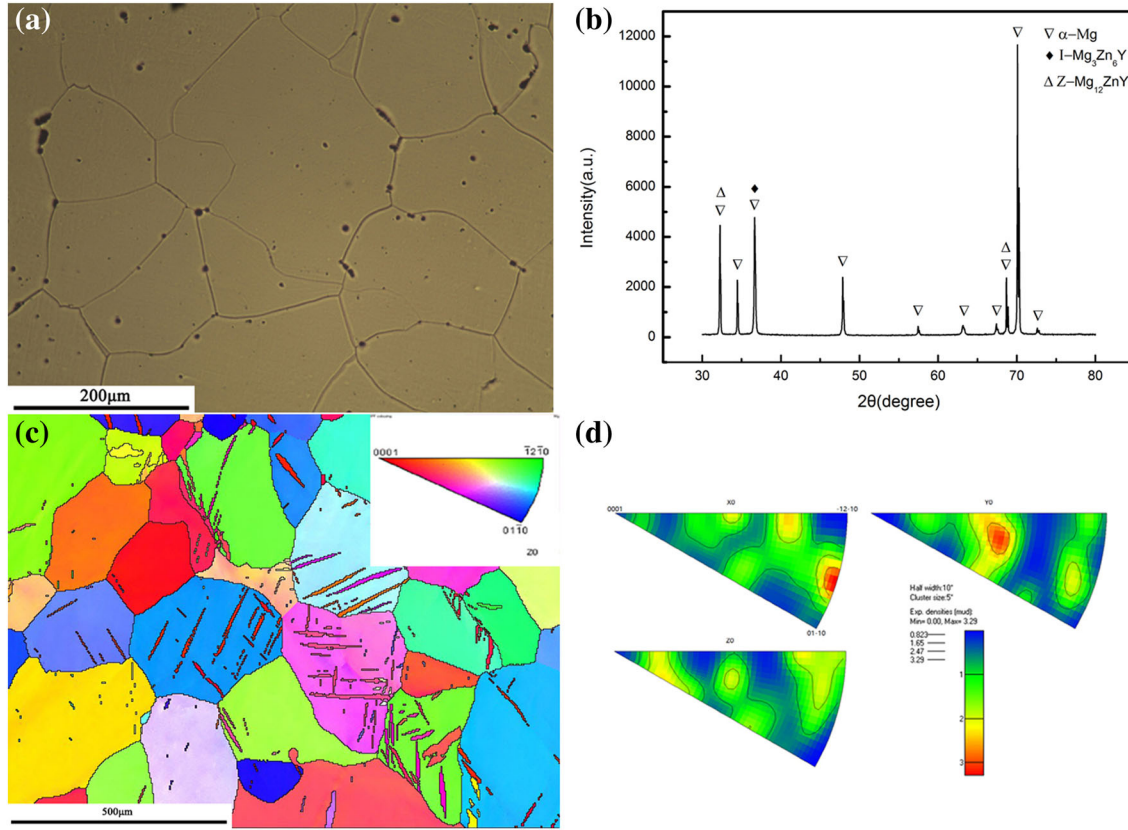
Fig. 1. Initial microstructure of the Mg-1.2Zn-0.2Y alloy: (a) optical microstructure; (b) XRD diagram; (c) EBSD map; (d) inverse pole figure.

finally reaching the maximum because of work hardening and working softening through dynamic recovery (DRV) and dynamic recrystallization (DRX). The detailed analysis through microstructure observation will be discussed in the following sections.

Constitutive Analysis

It is widely accepted that besides the material itself and heat treatment, the correlation among deformation temperature, strain rate and stress also varies with the degree of stress. For example, the relationship at lower and higher stress situations is described by Eqs. 1 and 2, respectively. Equation 3, proposed by Sellars and Tegart,[30–32] illustrates the relationship at all the stress levels.

$$\dot{\varepsilon} = A_1 \sigma^{n_1} \exp(-Q/RT) \qquad (1)$$

$$\dot{\varepsilon} = A_2 \exp(\beta\sigma) \exp(-Q/RT) \qquad (2)$$

$$\dot{\varepsilon} = A[\sinh(\alpha\sigma)]^n \exp(-Q/RT) \qquad (3)$$

where $\dot{\varepsilon}$ is the strain rate (s^{-1}); Q is the deformation activation energy; T is the absolute temperature (K); R is the gas constant (8.314 J mol^{-1} K^{-1}); σ is the peak stress (MPa); A_1, A_2, A, n_1, n, α and β are the structure factors; $\alpha = \beta/n_1$.

The relationship containing the Zener–Hollomon (Z) parameter can be shown as Eq. 4:[33]

$$Z = \dot{\varepsilon} \exp(Q/RT) = A[\sinh(\alpha\sigma)]^n \qquad (4)$$

By taking the natural log of both sides of Eqs. 1–4, we can get the following equations in turn:

$$\ln\dot{\varepsilon} = \ln A_1 + n_1 \ln\sigma - Q/RT \qquad (5)$$

$$\ln\dot{\varepsilon} = \ln A_2 + \beta\sigma - Q/RT \qquad (6)$$

$$\ln\dot{\varepsilon} = \ln A + n \ln[\sinh\alpha\sigma] - Q/RT \qquad (7)$$

$$\ln Z = \ln A + n \ln[\sinh\alpha\sigma] \qquad (8)$$

Figure 3a and b shows the linear relationships of $\ln\sigma - \ln\dot{\varepsilon}$ and $\sigma - \ln\dot{\varepsilon}$ at different temperatures. According to Eqs. 5 and 6, the values of $1/n_1$ and $1/\beta$ were the slope of the line in Fig. 3a and b,
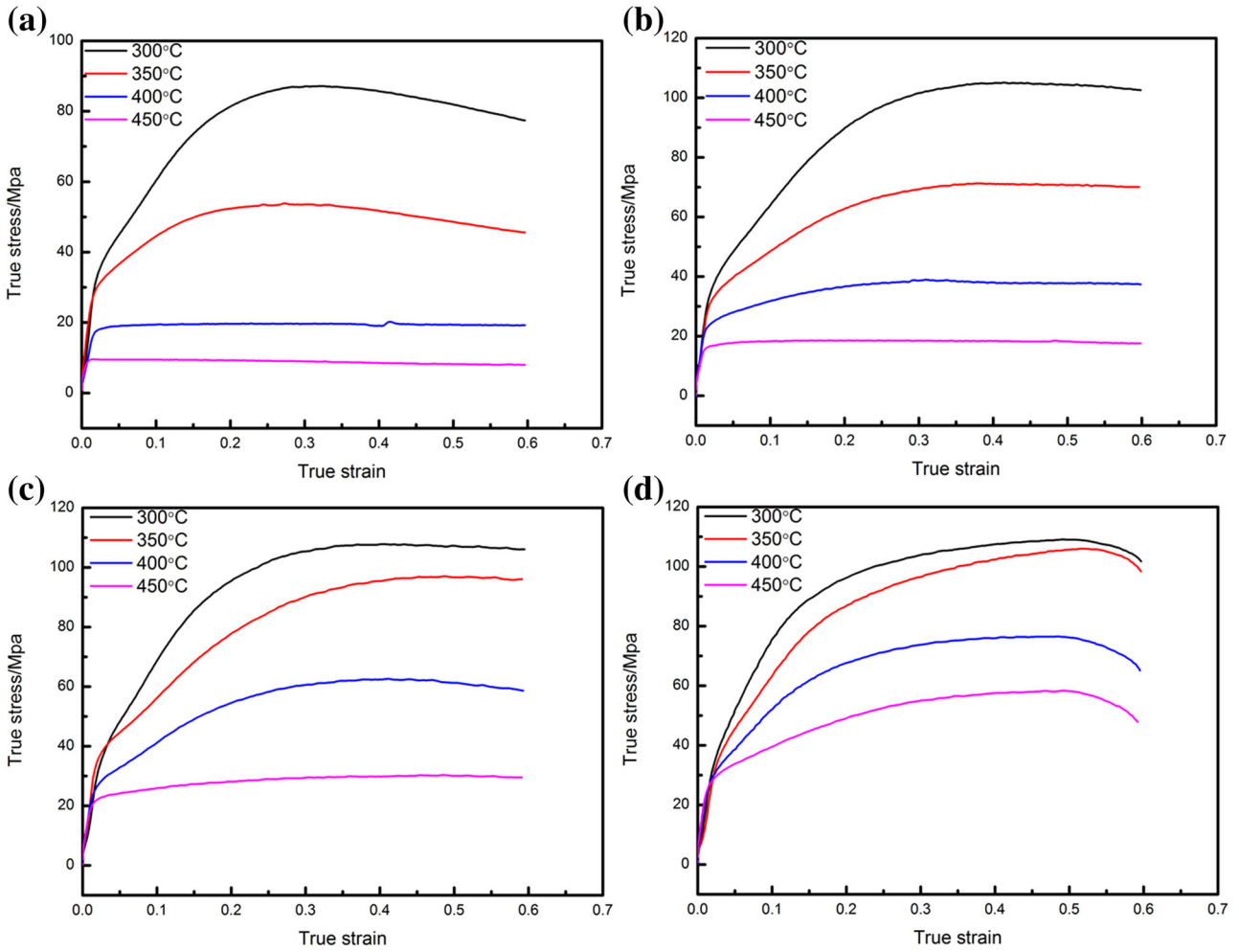
Fig. 2. True stress–true strain curves of the Mg-1.2Zn-0.2Y alloy during hot compression: (a) $\dot{\varepsilon} = 0.001$ s^{-1}; (b) $\dot{\varepsilon} = 0.01$ s^{-1}; (c) $\dot{\varepsilon} = 0.1$ s^{-1}; (d) $\dot{\varepsilon} = 1.0$ s^{-1}.

respectively. Therefore, the value of n_1 and β was calculated as $n_1 = 10.58235$ and $\beta = 0.15669$. Then, the mean value of α was obtained as 0.01487 according to $\alpha = \beta/n_1$.

By differentiating Eq. 7 with respect to $1/T$,

$$Q = R\{(\partial \ln \dot{\varepsilon})/\partial \ln[\sinh(\alpha\sigma)]\}_T \{\partial \ln[\sinh(\alpha\sigma)]/\partial(1/T)\}_{\dot{\varepsilon}} \tag{9}$$

The linear relationships of $\ln[\sinh \alpha\sigma] - \ln \dot{\varepsilon}$ and $1/T - \ln[\sinh(\alpha\sigma)]$ are fitted in Fig. 3c and d. According to Eq. 9, the slope values in Fig. 3c and d were the first and second part of Eq. 9, respectively. Therefore, the value of Q can be calculated to be 275.9 kJ/mol.

The linear relationship of $\ln[\sinh \alpha\sigma] - \ln Z$ is presented in Fig. 3e with a correlation coefficient of 0.973. The slope of the line in Fig. 3e can be viewed as the value of n, which is about 4.2597. The intercept of the fitted curve in Fig. 3e can be

observed as the value of $\ln A = 39.44391$, and then the value of A was calculated as 1.35×10^{17}.

By substituting the above parameters into Eq. 3, we can get:

$$\dot{\varepsilon} = 1.350 \times 10^{17}[\sinh(0.01487\sigma)]^{4.26} \exp(-275.9/8.314T) \tag{10}$$

then:

$$\sigma = \ln\Big\{ \big(Z/(1.35 \times 10^{17})\big)^{1/4.26} \\ + \big[(Z/(1.35 \times 10^{17}))^{(2/4.26+1)}\big]^{1/2} \Big\} \tag{11}$$

and in Eq. 11:

$$Z = \dot{\varepsilon} \exp(2.759 \times 10^5/RT) \tag{12}$$

The Q value is an important indicator to measure the difficulty of material deformation, which is related to the material itself and hot deformation
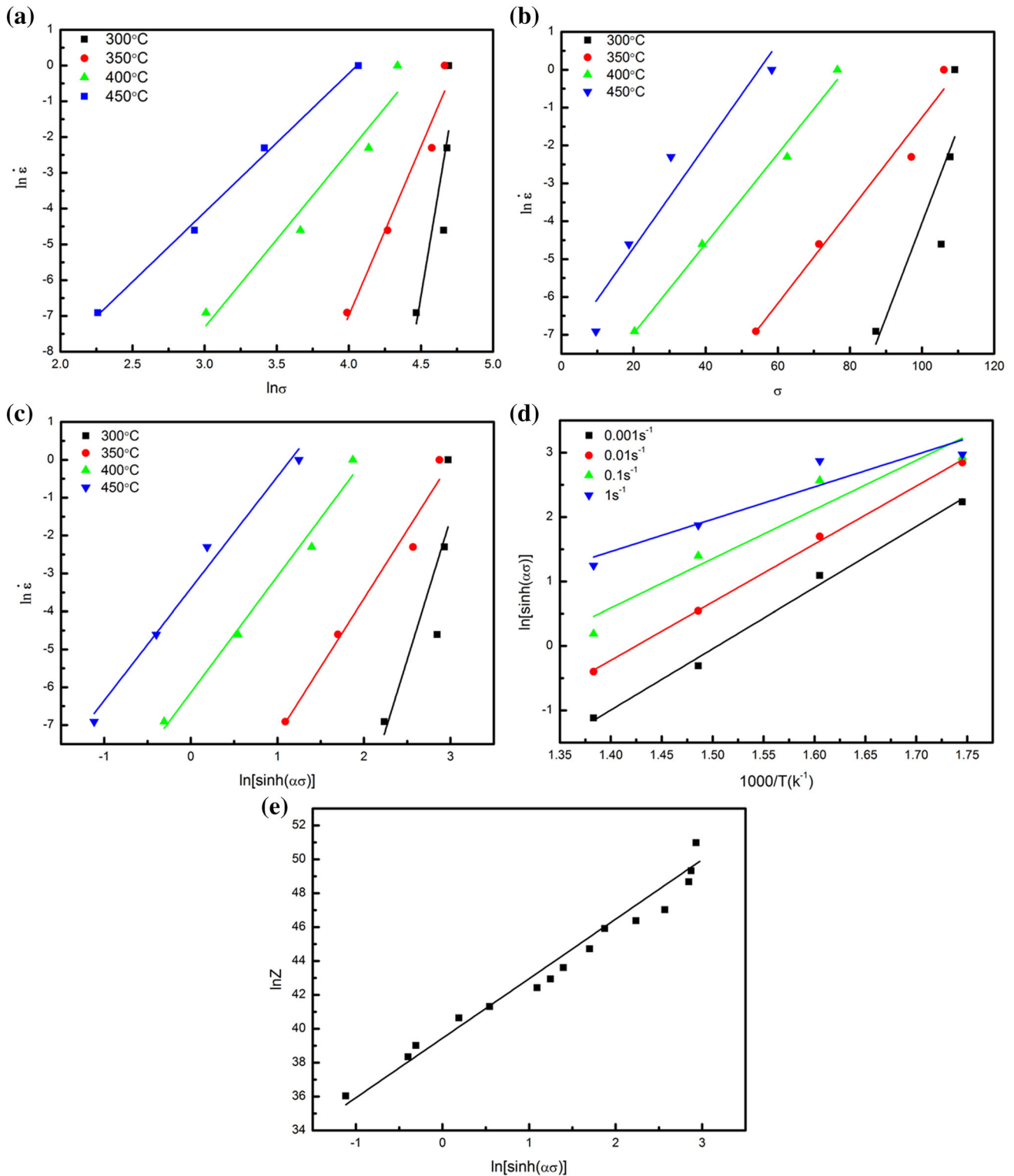
Fig. 3. Linear relationship fitting: (a) ln σ − ln $\dot{\varepsilon}$; (b) σ − ln $\dot{\varepsilon}$; (c) ln[sinh($\alpha\sigma$)] − ln $\dot{\varepsilon}$; (d) $T^{-1}/10^{-3}$K^{-1} − ln[sinh($\alpha\sigma$)]; (e) ln[sinh($\alpha\sigma$)] − ln Z.

parameters. Table I lists the Q values of pure Mg and Mg alloys. It is clear that the Q value of Mg alloys is higher than that of pure Mg, but the degree varies. And it is found that the Q value of the RE element-containing (i.e., Gd, Y) Mg alloys is much larger than that of pure Mg and other Mg alloys. The reason may be the addition of RE elements greatly increases Mg alloys' strength by solid solution strengthening and precipitation strengthening. Hence, the deformation of such Mg alloys is more

Table I. Comparison of Q values for Mg-1.2Zn-0.2Y alloy and other Mg alloys

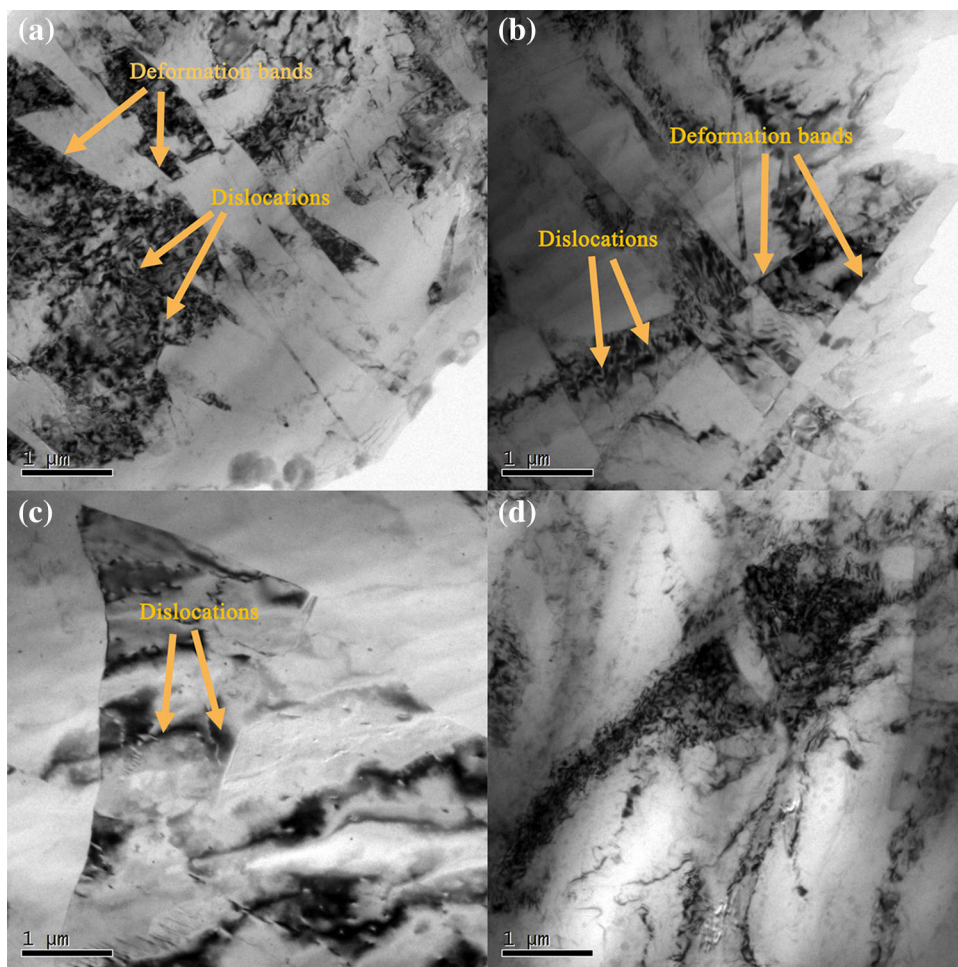| Materials	Q/KJmol^{-1}	References
Pure Mg	135	[34]
Mg-5.5Zn	177	[34]
Mg-5.5Zn-1.1Y	236	[34]
Mg-9.5Zn-2Y	176.3	[35]
Mg-5.75Zn-0.73Y-0.36Zr	251.2	[25]
Mg-2.0Zn-0.3Zr-0.9Y	236.2	[23]
Mg-6Zn-0.6Zr	140.3	[36]
Mg-9Al-1Zn	136.3	[37]
Mg-9Gd–2.4Y-0.4Zr	199.8	[37]
Mg-3Gd-1Zn	173.2	[5]
Mg-1.2Zn-0.2Y	275.9	The present work

Fig. 4. TEM images of the Mg-1.2Zn-0.2Y alloy deformed under various conditions: (a) ln$Z$ = 57.91 (300°C, 1 s^{-1}); (b) ln$Z$ = 50.96 (350°C, 0.1 s^{-1}); (c) ln$Z$ = 44.70 (400°C, 0.01 s^{-1}); (d) ln$Z$ = 38.99 (450 C, 0.001 s^{-1}).

difficult.[5,34,35,37] In the present Mg alloy, I-phase may be contained[25] and then increase the value of Q. In addition, the grain size of the present Mg-1.2Zn-0.2Y alloy is much larger ($\sim$ 300 μm), resulting in difficult slip during hot deformation. The overall deformation becomes more difficult, and then the larger Q value of the Mg-1.2Zn-0.2Y alloy is observed.
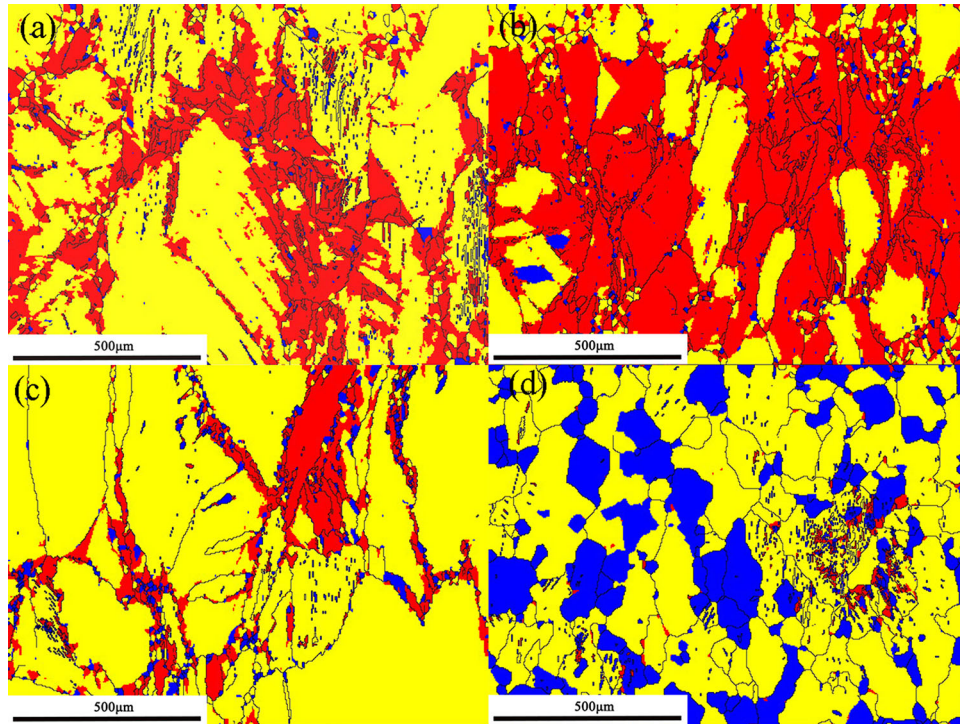
Fig. 5. DRX distribution images of the Mg-1.2Zn-0.2Y alloy after hot conditions: (a) $\ln Z = 57.91$ (300°C, 1 s^{-1}); (b) $\ln Z = 50.96$ (350°C, 0.1 s^{-1}); (c) $\ln Z = 44.70$ (400°C, 0.01 s^{-1}); (d) $\ln Z = 38.99$ (450°C, 0.001 s^{-1}).

Microstructure Characterization

In the process of hot deformation of metal materials, different deformation parameters often lead to different deformation mechanisms and deformation microstructures. The TEM images of the Mg-1.2Zn-0.2Y alloy deformed under various conditions are presented in Fig. 4. From Fig. 4a and b, it can be found that many deformation bands were formed in some larger grains. It is a fact that the crystal structure of the Mg alloy is HCP with limited slip systems, which always results in poor workability at low temperature. Especially at high strain rates, it is easy to generate uneven stress in some larger grains and eventually form deformation bands. In addition, many dislocations can be found in some deformation bands, which can be ascribed to the soft orientation of the grains. During compression deformation, the density of dislocation increased continuously, and a large amount of dislocation accumulated in the grains, resulting in the formation of complex cell-like entangled structures. However, in some grains with hard orientation, there was almost no dislocation, which can be attributed to the moving difficulty of the slip system in these grains. With the increase of deformation temperature, the mobility of dislocations increased, and the slip activated in the grains with soft orientation. At the same time, the rearrangement and annihilation of dislocations were easier, generally leading to the

decrease of dislocation density, as shown in Fig. 4c. With the further movement and interaction of dislocations, clear grain boundaries gradually formed (Fig. 4d). This phenomenon has been confirmed in many references.[38]

The EBSD images of the Mg-1.2Zn-0.2Y alloy after hot deformation are presented in Fig. 5. The blue, yellow and red colors represent DRX grains, sub-microstructures and deformed grains, respectively. Many sub-microstructures are formed under various deformation conditions, and Fig. 5a–c shows that dislocation entanglement is formed, which is a typical DRV structure. However, at the condition of 450°C and 0.001 s^{-1} DRX grains accounted for a larger proportion. This can be attributed to the high thermal deformation activation energy of the tested alloy. In addition, high deformation temperature and low strain rate provided conditions for DRX. Therefore, the main softening mechanism could be summarized as DRV and DRX, and DRX mainly occurred under low strain rate and high temperature deformation conditions.

Compared with the homogenized alloy (Fig. 1c), it can be found that the equiaxed crystals almost disappeared and the grains were elongated (Fig. 5a-c). In addition, a small number of fine recrystallized grains were formed at the grain boundaries. When deformed at 450°C and 0.001 s^{-1}, the deformed grains re-formed equiaxed grains through DRX, and
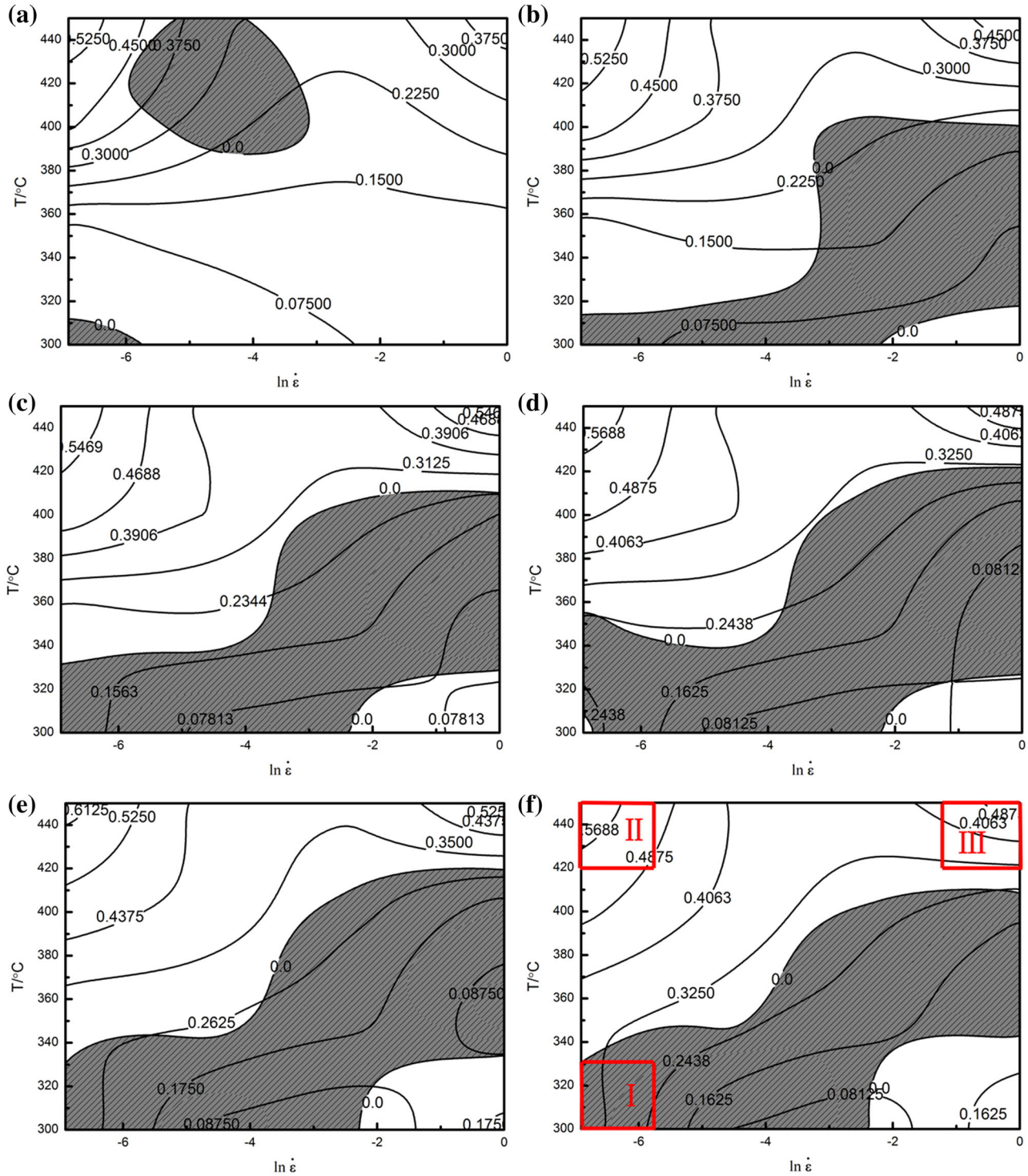
Fig. 6. Processing maps of the Mg-1.2Zn-0.2Y alloy at strains of (a) 0.1; (b) 0.2; (c) 0.3; (d) 0.4; (e) 0.5; (f) 0.6.

the grain size was reduced from 300 μm before deformation to about 100 μm (Fig. 5d).

The misorientation distribution of the Mg-1.2Zn-0.2Y alloy at various conditions is presented in supplementary Fig. S-1. In the case of 350°C and 1 s^{-1}, the ratio of high-angle grain boundaries

(HAGBs) and the average misorientation angle were 78.4% and 34.85°, respectively. However, the corresponding values at the condition of 450°C and 0.001 s^{-1} were 82.6% and 45.69°, respectively. This means that the formation of DRX grains greatly improves the proportion of HAGBs.
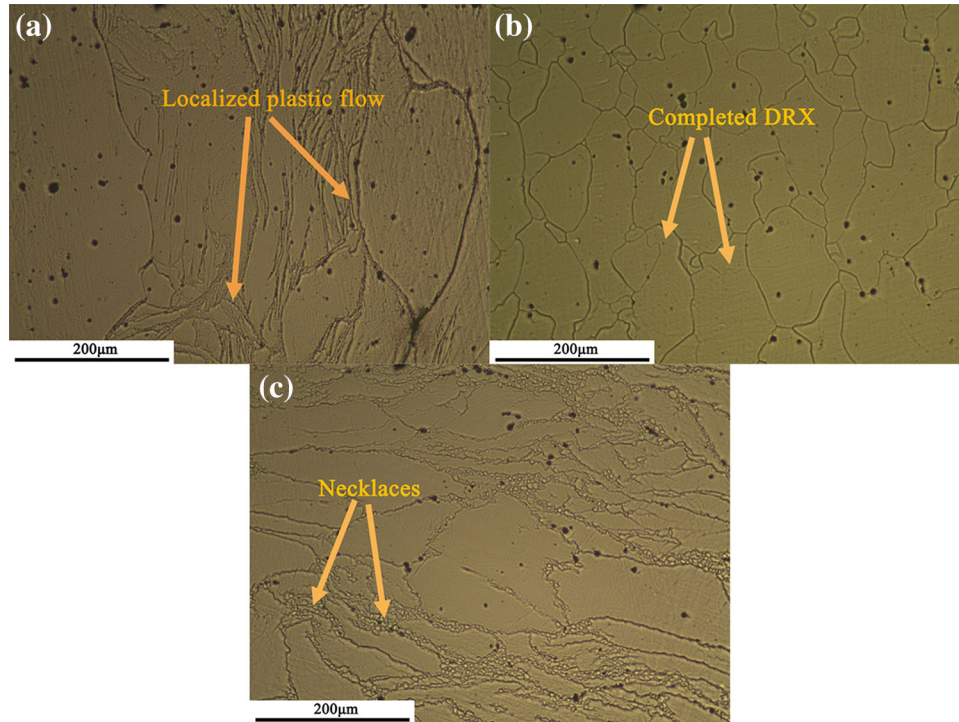
Fig. 7. The optical microstructure of the Mg-1.2Zn-0.2Y alloy at various processing conditions: (a) 300°C, 0.001 s^{-1}; (b) 450°C, 0.001 s^{-1}; (c) 450°C, 1 s^{-1}.

Processing Maps

The obtained data of hot compression tests can be also utilized to construct processing maps based on dynamic materials modeling (DMM). The processing map can be used to investigate the hot workability and optimize the hot processing parameters of the materials. According to this model, the work piece can be described as a dissipater of power in the total processing system. The dissipated power consists of two parts, as shown in the following equation:

$$P = \sigma\dot{\varepsilon} = G + J = \int_0^{\dot{\varepsilon}} \sigma d\dot{\varepsilon} + \int_0^{\sigma} \dot{\varepsilon} d\sigma \qquad (13)$$

where the G content refers to the power dissipated via plastic working, most of which is converted into heat. The J co-content refers to the power dissipated by metallurgical processes, such as DRV, DRX, phase transformation and cracking.[39–41]

From Eq. 13, the strain rate sensitivity parameter (m) of the flow stress can be used to describe the relationship between G and J:

$$\begin{aligned} \mathrm{d}J/\mathrm{d}G &= (\partial P/\partial G)(\partial J/\partial P) = (\dot{\varepsilon}\mathrm{d}\sigma)/(\sigma\mathrm{d}\dot{\varepsilon}) \\ &= \partial(\ln\sigma)/\partial(\ln\dot{\varepsilon}) = m \end{aligned} \qquad (14)$$

At an ideal dissipation condition ($m = 1$), J can reach to its maximum:

$$J = J_{\max} = \sigma\dot{\varepsilon}/2 \qquad (15)$$

In general, the dissipative power factor η is defined as J/Jmax:

$$\eta = J/J_{\max} = [m\sigma\dot{\varepsilon}/(m+1)]/(\sigma\dot{\varepsilon}/2) = 2m/(m+1) \qquad (16)$$

The dimensionless parameter (η) characterizes the efficiency of dissipating energy by microstructure changes. Meanwhile, the instability map can be developed on the basis of the extreme principles of irreversible thermodynamics.[42] The instability criterion is defined as:

$$\xi(\dot{\varepsilon}) = \partial\ln(m/(m+1))/\partial\ln\dot{\varepsilon} + m < 0 \qquad (17)$$

According to Eq. 17, the flow instability region at various conditions can be drawn, which is called the instability graph.

By superimposing the instability map on the power dissipation map, the processing maps at different strains can be constructed, which directly reflects the suitable and non-suitable processing zones. The processing maps of the Mg-1.2Zn-0.2Y alloy at different strains are presented in Fig. 6. The shadow areas represent the rheologic instability domains, and the other areas are the safety processing domains. Obviously, when the strain increased from 0.2 to 0.6, there was no marked change in the processing maps. The strain parameter did not significantly change the distribution and interval size of the hot-working drawing range

of Mg alloys, and the direction of power dissipation efficiency and its contour lines were not significantly affected. Figure 2 also indicated that when the strain was 0.1, the tested alloy was still in the processing hardening stage. The equilibrium state between work hardening and dynamic restoration was gradually reached when the strain exceeded 0.2. From the processing maps, we can see that the rheologic instability zones were mainly located at 300–350°C, 0.001–1.0 s^{-1} and 350–420°C, 0.01–1.0 s^{-1}. The value of the contour line represents the energy dissipation factor η. Generally, the field with the energy dissipation coefficient > 0.3 is suitable for hot processing. However, as the high energy dissipation rate is also related to the wedge crack failure mechanism, the analysis of the processing map needs to be supported by microstructure analysis.

In addition to reflecting suitable and unsuitable processing zones, the processing maps potentially express different deformation mechanisms under different deformation conditions. Accordingly, different deformation mechanisms will lead to different deformation microstructures. Taking Fig. 6f as an example, three typical areas were selected for the microstructure observation. Figure 7 shows the optical microstructures of the Mg-1.2Zn-0.2Y alloy processed under various conditions, and Fig. 7a indicates that in the unstable deformation zone with 300°C and 0.001 s^{-1} (Domain I), the grains were elongated and localized plastic flow appeared in local areas. This is the typical instability mechanism for metal materials deformed at high strain rates and low temperatures.[43]

In addition, Fig. 7b shows that under the appropriate condition of 450°C and 0.001 s^{-1} (Domain II), the DRX process was more adequate and eventually fine DRXed grains formed.

However, as shown in Fig. 7c, in Domain III, corresponding to the stability domain with high temperature and high strain rate, the microstructure obviously consisted of new necklace-like grains along the original grain boundaries, which is a typical inadequate recrystallization microstructure. It is well known that the recrystallization process is controlled by the rates of nucleation and growth. For polycrystalline Mg alloys, recrystallization nucleation tends to occur in the intersection of deformation bands and/or twins, and then DRXed grains grow by migration of the original grain boundaries.[44] The whole process is controlled by recrystallization activation energy and the driving energy for grain boundary migration. At higher strain rate conditions, the lack of sufficient recrystallization growth time leads to the formation of a necklace-like microstructure. This microstructure tends to evolve into an instability structure because of flow localization. In general, the optimum processing parameters presented on the processing map were 420–450°C and 0.001–0.01 s^{-1}, with a peak efficiency of power dissipation of about 56.88%.

CONCLUSION

Flow stress behavior of as-cast dilute Mg-1.2Zn-0.2Y alloy was investigated by the uniaxial thermal compression test using a Gleeble-3500 test system. Constitutive equations and processing maps were established for the tested Mg alloy. The main conclusions can be drawn as:

1. The true stress–true strain curves showed typical dynamic recovery characteristics. The flow stress decreased with the increase of deforming temperature and increased with the increase of strain rate.
2. The deformation activation energy Q of the Mg-1.2Zn-0.2Y alloy was calculated to be 275.9 kJ/mol, and the constitutive equation can be established as:

$$\sigma = \ln\left\{ \left(Z/\left(1.35 \times 10^{17}\right)\right)^{1/4.26} + \left[\left(Z/\left(1.35 \times 10^{17}\right)\right)^{(2/4.26+1)}\right]^{1/2}\right\}. \quad (18)$$

3. Dynamic recovery (DRV) was the main softening mechanism of the Mg-1.2Zn-0.2Y alloy during deformation at lower temperature, and dynamic recrystallization (DRX) mainly occurred at higher temperature.
4. The optimum processing zone was located at 420–450°C and 0.001–0.01 s^{-1}, with a peak η of 56.88%.

ACKNOWLEDGEMENTS

ELECTRONIC SUPPLEMENTARY MATERIAL

The online version of this article (https://doi.org/10.1007/s11837-019-03659-6) contains supplementary material, which is available to authorized users.

REFERENCES

1. Z. Yang, J. Li, J. Zhang, and G.W. Lorimer, *Acta Metall.* 21, 313 (2008).
2. N. Mo, Q. Tan, and M. Bermingham, *Mater. Des.* 155, 422 (2018).
3. S. Tekumalla, S. Seetharaman, A. Almajid, and M. Gupta, *Metals* 5, 1 (2015).

4. H. Yua, H. Yan, J. Chen, B. Su, Y. Zheng, Y. Shen, and Z. Ma, *J. Alloys Compd.* 586, 757 (2014).
5. M. Roostaei, M.H. Parsa, R. Mahmudi, and H. Mirzadeh, *J. Alloys Compd.* 631, 1 (2015).
6. B. Pourbahari, H. Mirzadeh, and M. Emamy, *J. Mater. Eng. Perform.* 27, 1327 (2018).
7. B. Pourbahari, H. Mirzadeh, and M. Emamy, *Mater. Sci. Eng., A* 680, 39 (2017).
8. Y. Zhang, X. Zeng, L. Liu, L. Chen, H. Zhou, Q. Li, and Y. Zhu, *Mater. Sci. Eng., A* 373, 320 (2004).
9. M. Socjusz-Podosek and L. Lity nska, *Mater. Chem. Phys.* 80, 472 (2003).
10. D. Xu, W. Tang, L. Liu, Y. Xu, and E. Han, *J. Alloys Compd.* 432, 129 (2007).
11. J.Y. Lee, H.K. Lim, D.H. Kim, and W.T. Kim, *Mater. Sci. Eng., A* 491, 349 (2008).
12. Z. Zhang, X. Liu, W. Hu, J. Li, Q. Le, L. Bao, Z. Zhu, and J. Cui, *J. Alloys Compd.* 624, 116 (2015).
13. A. Müller, G. Garcés, P. Pérez, and P. Adeva, *J. Alloys Compd.* 443, L1 (2007).
14. D.H. Bae, M.H. Lee, and K.T. Kim, *J. Alloys Compd.* 342, 445 (2002).
15. D.H. Bae, S.H. Kim, and D.H. Kim, *Acta Mater.* 50, 2343 (2002).
16. M. Jiang, C. Xu, T. Nakata, H. Yan, R. Chen, and S. Kamado, *Mater. Sci. Eng., A* 678, 329 (2016).
17. M. Jiang, C. Xu, and T. Nakata, *J. Alloys Compd.* 668, 13 (2016).
18. H. Mirzadeh, *Mech. Mater.* 77, 80 (2014).
19. M. Karami and R. Mahmudi, *Mater. Lett.* 81, 235 (2012).
20. H. Mirzadeh and A. Najafizadeh, *Mater. Des.* 31, 1174 (2010).
21. J. Yu, Z. Zhang, Q. Wang, X. Yin, J. Cui, and H. Qi, *J. Alloys Compd.* 704, 382 (2017).
22. Z. Zhang, X. Yang, Z. Xiao, J. Wang, D. Zhang, C. Liu, and T. Sakai, *Mater. Des.* 97, 25 (2016).
23. B. Lva, J. Peng, Y. Wang, X. An, L. Zhong, A. Tang, and F. Pan, *Mater. Des.* 53, 357 (2014).
24. X. Xia, Q. Chen, S. Huang, J. Lin, C. Hu, and Z. Zhao, *J. Alloys Compd.* 644, 308 (2015).
25. Q. Chen, X. Xia, B. Yuan, D. Shu, Z. Zhao, and J. Han, *Mater. Sci. Eng., A* 593, 38 (2014).
26. Y.V.R.K. Prasad and K.P. Rao, *Mater. Sci. Eng., A* 487, 316 (2008).
27. S. Aliakbari Sani, G.R. Ebrahimi, and A.R. Kiani Rashid, *J. Alloys Compd.* 4, 104 (2016).
28. G. Quan, T. Ku, and W. Song, *Mater. Des.* 32, 2462 (2011).
29. J. Li, J. Liu, and Z. Cui, *Mater. Des.* 56, 889 (2014).
30. C.M. Sellars and W.J. McTegart, *Acta Metall.* 14, 1136 (1966).
31. H. McQueen and N. Ryan, *Mater. Sci. Eng., A* 322, 43 (2002).
32. M.A. Jabbari Taleghani, E.M. Ruiz Navas, M. Salehi, and J.M. Torralba, *Mater. Sci. Eng., A* 534, 624 (2012).
33. D. Ponge and G. Gottstein, *Acta Mater.* 46, 69 (1998).
34. M. Chaman-ara, G.R. Ebrahimi, and H.R. Ezatpour, *Trans. Nonferrous Metals Soc. China* 28, 629 (2018).
35. T.Y. Kwak, H.K. Lim, and W.J. Kim, *J. Alloys Compd.* 644, 645 (2015).
36. H. Mirzadeh, *Mater. Chem. Phys.* 152, 123 (2015).
37. H. Mirzadeh, *J. Mater. Res.* 5, 1 (2016).
38. A. Rollett, F. Humphreys, G.S. Rohrer, and M. Hatherly, *Recrystallization and Related Annealing Phenomena*, 2nd ed. (Pergamon: Elsevier, 2004), pp. 219–224.
39. Y.V.R.K. Prasad, H.L. Gegel, S.M. Doraivelu, J.C. Malas, J.T. Morgan, and K.A. Lark, *Metall. Trans. A* 15, 1883 (1984).
40. O. Sivakesavam and Y.V.R.K. Prasad, *Mater. Sci. Eng., A* 362, 118 (2003).
41. X. Xia, Q. Chen, and K. Zhang, *Mater. Sci. Eng., A* 587, 283 (2013).
42. Y.V.R.K. Prasad, *Indian J. Technol.* 28, 435 (1990).
43. Z. Zhang, H. Zhou, and X. Liu, *Mater. Sci. Eng., A* 565, 213 (2013).
44. S.G. Hong, S.H. Park, and C.S. Lee, *Scr. Mater.* 64, 145 (2011).